Engineering xxx (xxxx) xxx

Contents lists available at ScienceDirect

Engineering

journal homepage: www.elsevier.com/locate/eng

Research
Energy System Engineering—Article

A High-Efficiency Off-Axis Space Solar Concentrator with Large Tolerance for Acceptance Angle Variations

Yanlong Zhang [a], Pengzhen Guo [b,*], Mengfan Tian [b], Yun Chen [a], Zin Min Khant [a], Yiming Kong [a], Dingkun Gao [a], Linghao Li [a], Hongwei Guo [a], Rongqiang Liu [a], Zongquan Deng [a], Lifang Li [c,*]

[a] National Key Laboratory of Aerospace Mechanism, Harbin Institute of Technology, Harbin, 150001, China
[b] National Key Laboratory of Laser Spatial Information, Harbin Institute of Technology, Harbin, 150001, China
[c] State Key Laboratory of Space Environment and Matter Interaction, Harbin Institute of Technology, Harbin, 150001, China

ARTICLE INFO

Article history:
Received 19 September 2025
Revised 30 December 2025
Accepted 11 August 2026
Available online xxxx

Keywords:
Aberration compensation
Solar concentrator
High concentration ratio
Deep space exploration

ABSTRACT

The use of solar energy for lunar regolith melting plays a key role in the construction of lunar bases and *in-situ* resource utilization. In this process, solar concentrators should achieve high efficiency while minimizing the reliance on precise solar tracking, which helps reduce installation costs and precision requirements during space exploration. In this work, we propose an off-axis conjugate point-focus solar concentrator that combines a zero-occlusion triple-mirror configuration with aberration-compensated freeform surfaces to enhance both concentration performance and angular acceptance. The 300 mm-aperture system is optimized to maintain efficient focusing within an acceptance half-angle of ±0.5°, where the acceptance angle is defined as the maximum incidence-angle deviation from the ideal normal incidence for which the concentration ratio remains above 90% of its on-axis value, representing roughly a two-fold improvement in angular tolerance compared with conventional off-axis dish concentrators reported in the literature, while keeping a higher concentration ratio. A feedback-based optical design method is developed, in which a conjugate mirror and iterative adjustment of the mirror normals are used to suppress coma and spherical aberrations and improve the focal-spot energy distribution. Monte Carlo ray-tracing and aberration analysis show that the optimized design achieves a high optical concentration ratio and a compact focal spot with low residual aberrations over the design field of view. Outdoor solar concentration experiments under a solar irradiance of 390 $W \cdot m^{-2}$ and an ambient temperature of 5 °C demonstrate a peak focal temperature of 892 °C and an effective concentration ratio of 548. Under lunar irradiance with radiative boundary conditions, the model predicts a focal temperature of 1326 °C, which is competitive with previously reported off-axis concentrator systems designed for space applications. These results indicate that the proposed concentrator can provide the high-temperature flux required for lunar regolith melting and other *in-situ* resource utilization (ISRU) processes, and that its enhanced angular tolerance makes it well suited for deployment on lunar surface platforms and deep-space energy systems.

© 2026 THE AUTHORS. Published by Elsevier LTD on behalf of Chinese Academy of Engineering and Higher Education Press Limited Company. This is an open access article under the CC BY-NC-ND license (http://creativecommons.org/licenses/by-nc-nd/4.0/).

1. Introduction

The utilization of *in-situ* resource utilization (ISRU) is fundamental to establishing sustainable lunar bases, as it reduces reliance on Earth-supplied materials and enables long-term extraterrestrial operations. Among ISRU techniques, lunar regolith melting plays a critical role in producing essential construction materials such as lunar bricks, which are key to infrastructure development [1]. As lunar exploration progresses toward long-term habitation, the demand for highly efficient and renewable energy solutions has become increasingly significant [1,2]. Due to its abundance and continuous availability, solar energy stands out as the most viable power source for supporting ISRU processes and sustaining lunar infrastructure [3,4]. The advancement of solar concentrator technologies [5] has further enhanced the feasibility of solar-driven regolith melting by enabling effective thermal

* Corresponding authors.
E-mail addresses: guopengzhen@hit.edu.cn (P. Guo), lilifang@hit.edu.cn (L. Li).

https://doi.org/10.1016/j.eng.2026.08.029
2095-8099/© 2026 THE AUTHORS. Published by Elsevier LTD on behalf of Chinese Academy of Engineering and Higher Education Press Limited Company.
This is an open access article under the CC BY-NC-ND license (http://creativecommons.org/licenses/by-nc-nd/4.0/).

Please cite this article as: Y. Zhang, P. Guo, M. Tian et al., A High-Efficiency Off-Axis Space Solar Concentrator with Large Tolerance for Acceptance Angle Variations, Engineering, https://doi.org/10.1016/j.eng.2026.08.029

energy utilization [6,7]. By focusing high-intensity solar flux, these systems provide a direct and efficient approach to achieving the elevated temperatures required for lunar regolith processing.

Due to the Moon's synchronous rotation (sidereal period of 27.3 days; synodic day of ~29.5 days) and small axial tilt (~1.5°), solar illumination at a fixed site changes slowly but over a wide range during a lunar day [8,9]. In polar regions, the Sun remains at low elevation, and the combination of low solar altitude and rugged topography leads to complex local incidence angles; even small pointing or siting errors can shift the beam away from the nominal direction by tenths of a degree to several degrees [10]. In addition, the lunar surface experiences extreme thermal cycles, from cryogenic conditions below 40 K in permanently shadowed regions to peak daytime temperatures around 390–400 K at low-latitude noon [11,12]. These illumination and thermal conditions require solar concentrators that can maintain a high concentration ratio while tolerating realistic pointing errors and thermally induced structural deformations, especially for long-duration ISRU operations.

Despite its potential, developing an optimized solar concentrator for lunar applications presents several engineering and operational challenges. A well-designed system must achieve high optical concentration while maintaining robustness against tracking deviations [6]. Various solar concentrator architectures, including parabolic troughs, central receiver towers, and dish concentrators, have been explored, with dish-based concentrators demonstrating superior geometric concentration ratios, higher focal temperatures, and minimized cosine losses [13–15]. These features make dish concentrators particularly suitable for lunar thermal applications. However, conventional dish concentrators rely on large-scale segmented mirrors supported by complex structural frameworks, increasing both weight and deployment difficulty [16]. Additionally, maximizing the concentration ratio requires high reflector surface accuracy and minimized absorber size, leading to stringent engineering constraints. Improving reflector precision often demands reinforced structural support, further increasing system mass and reducing adaptability for extraterrestrial deployment [17].

Various studies have explored different secondary reflector configurations to mitigate optical losses and improve concentration efficiency. Dual-mirror systems, for example, have been optimized through precise optical alignment strategies to enhance concentration ratios and improve system performance. Adaptive secondary reflector designs have also been proposed, in which portions of the reflected rays are redirected back to the absorber, improving optical efficiency while ensuring uniform energy distribution [18,19]. However, such approaches require extremely precise solar tracking mechanisms, as small misalignments significantly affect the concentrator's effectiveness. Additionally, secondary reflectors have been implemented in parabolic trough concentrators, where they help maintain a stable focal-to-diameter ratio along a linear receiver, effectively controlling the shape of the focal spot [20,21]. While these configurations offer a broader acceptance angle, their concentration ratios remain lower than those of dish concentrators, limiting their effectiveness in high-intensity thermal applications such as regolith melting.

Current space-based solar concentrators typically fall into two major categories: Wide field-of-view, low-concentration systems that tolerate tracking deviations but suffer from low thermal efficiency, and high-concentration, narrow-tolerance systems that maximize solar flux density but are highly sensitive to tracking errors [20]. Neither of these designs fully satisfies the requirements for a sustainable lunar base, where both high concentration and robust tracking tolerance are essential. Practical challenges such as alignment errors, non-ideal solar divergence, and optical aberrations contribute to focal spot distortions and uneven energy flux distribution, negatively impacting system performance [21,22]. Spherical and chromatic aberrations further degrade optical efficiency, especially in off-axis concentrator configurations, where deviations in the focal-to-diameter ratio and off-axis distance increase the system's susceptibility to aberrations [23,24]. Existing approaches to mitigate these effects rely on computationally intensive global optimization techniques and ray-tracing simulations. While effective, these methods introduce high computational costs and require extensive parameter tuning. Alternative approaches, such as ray incidence angle optimization, provide a more practical means of analyzing optical sensitivity, but they do not fully address the impact of optical aberrations on concentrator performance [25,26]. Other research has proposed low-collimation sensitivity optical design methods based on nodal aberration theory, which examine how changes in optical system parameters influence performance [27–29]. Despite these advancements, existing concentrator technologies remain suboptimal for lunar applications due to their limited angular acceptance, sensitivity to tracking deviations, and high computational demands for optimization [30].

This study presents an innovative off-axis conjugate point-focus solar concentrator design, optimized through aberration compensation, offering a novel solution for sustainable lunar base construction and ISRU. Conventional off-axis dish concentrators for lunar thermal applications typically achieve geometric concentration ratios of approximately 200–300, with angular acceptance half-angles generally below 0.2°–0.3°. In contrast, the concentrator developed in this work is designed to maintain a comparable or higher optical concentration ratio while extending the effective acceptance half-angle to ±0.5°. This combination of high concentration and enlarged angular tolerance directly addresses the tracking and alignment constraints of compact lunar solar power systems. We analyze the variation in focal spots of off-axis concentrators within a limited field of view and identify the key factors that contribute to efficiency loss. Weighted adjustments and multi-angle light-path corrections are then introduced, while the aberrations induced by the off-axis design are compensated using a conjugate mirror, enabling precise control of the focal spot shape and enhancing both the concentration ratio and overall efficiency. Finally, outdoor solar concentration experiments are carried out to validate the performance of the proposed design under real illumination conditions.

2. Mathematical and physical model

As shown in Fig. 1(a), the three-dimensional model of the off-axis conjugate concentrator comprises an off-axis triple-mirror system and a dual-axis solar tracker. The optical structure of the off-axis triple-mirror system consists of three components: an off-axis concentrator, a co-focusing conjugate secondary mirror, and a plane reflector. When sunlight strikes the off-axis concentrator, its off-axis reflective surface first captures and concentrates the sunlight, which is then reflected to the conjugate mirror located off the optical axis. This design effectively avoids occlusion of the primary mirror by the receiving surface and conjugate mirror in the main optical path. The conjugate mirror is positioned between the reflective surface of the off-axis concentrator and the virtual focal point. Through this secondary reflection, it compensates optical aberrations and optimizes the main optical path, thereby enhancing the system concentration ratio. The plane mirror is placed in the secondary compensated reflection path, and by rotating this mirror, the optical path can be precisely adjusted, ensuring that the light accurately reaches the target focal point.

2.1. Off-axis concentrator design

The design of a coaxial concentrator primarily consists of a primary coaxial mirror and a receiving surface positioned directly

Please cite this article as: Y. Zhang, P. Guo, M. Tian et al., A High-Efficiency Off-Axis Space Solar Concentrator with Large Tolerance for Acceptance Angle Variations, Engineering, https://doi.org/10.1016/j.eng.2026.08.029

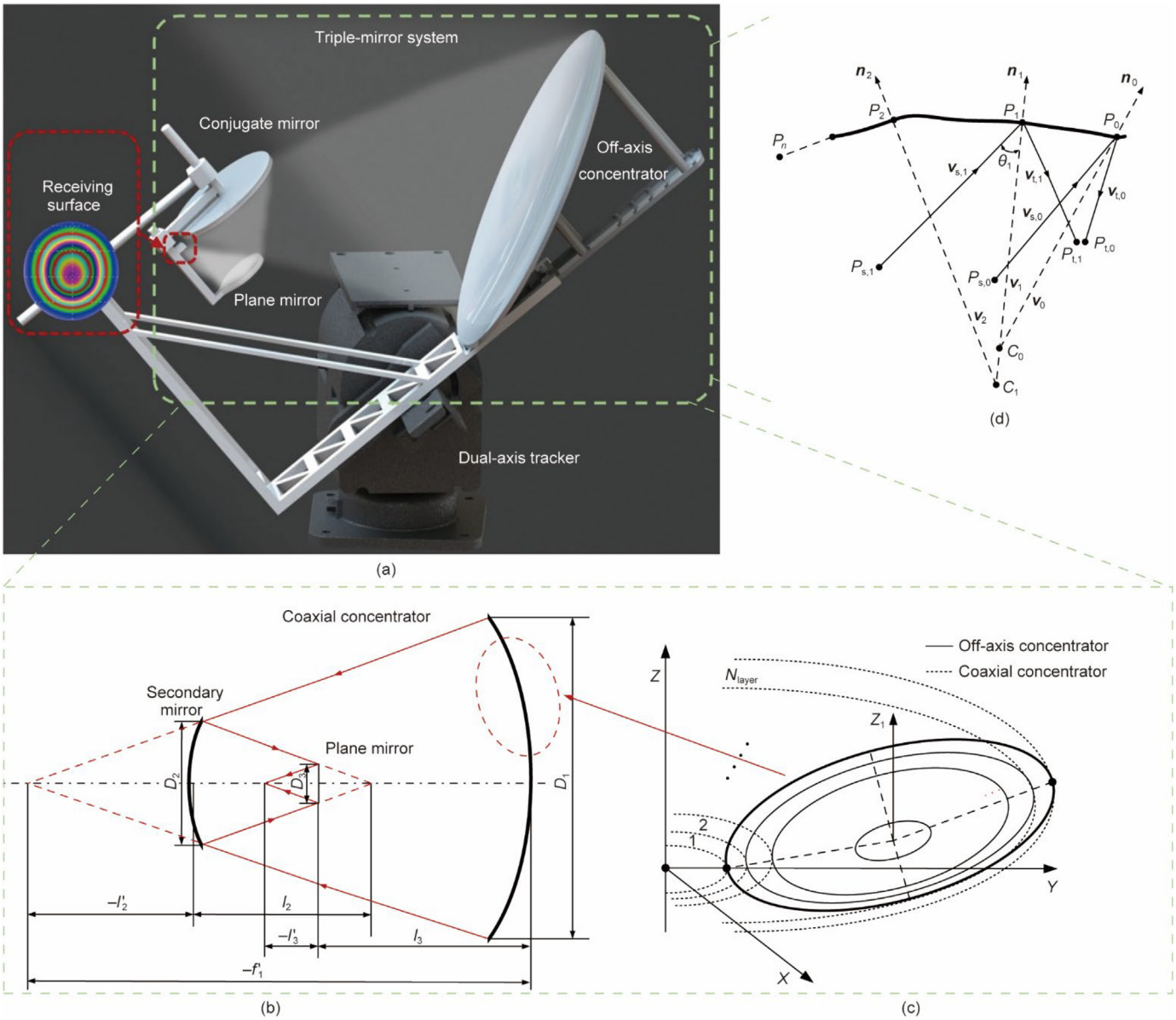


Fig. 1. Design of the off-axis conjugate concentrator: (a) three-dimensional model of the off-axis conjugate concentrator; (b) dimensions of the triple-reflection coaxial concentrator, D_1, D_2, D_3 denote the diameters of the primary, secondary, and tertiary mirrors, respectively; f'_1 is the focal length of the primary mirror, l_2 and l'_2 denote the conjugate distances used in defining the corresponding magnification, l_3 and l'_3 denote the axial distances associated with the subsequent folded reflection path; (c) schematic diagram of the concentrator's layering, X, Y, and Z define the concentrator coordinate system, respectively; Z_1 denotes the axial coordinate of the off-axis reflective surface; (d) construction process of the concentrator's reflective surface, $P_{s,i}$, P_i, and $P_{t,i}$ denote the source point, surface-intersection point, and target point of the ith ray ($i = 0, 1, 2, \ldots, n$), respectively; $v_{s,i}$ and $v_{t,i}$ are the corresponding incident- and target-direction vectors, respectively; n_i is the surface normal; C_i denotes the center of the corresponding circular-arc segment; and $[\mathrm{GRKSLT}]_i$ is the rotation angle used in determining the surface normal.

above its optical axis. To enhance the concentration efficiency, an auxiliary secondary mirror is typically introduced into the design for secondary focusing. Moreover, for precise adjustment of the focal point, a rotatable plane mirror can be integrated into the secondary focusing optical path, forming a triple-reflection optical system. This design allows light to undergo three reflections, achieving a higher concentration ratio and improved light control. In the analytical model (Fig. 1(b)), all reflective surfaces are initially approximated by rotationally symmetric quadratic conic surfaces, which is appropriate for the coaxial parent design and enables the use of third-order aberration formulas. Higher-order freeform departures are then introduced numerically in Sections 2.2 and 2.3 to further suppress residual aberrations. This modeling choice follows the classical third-order aberration theory of coaxial three-mirror systems [31–33], in which each mirror is modeled as a rotationally symmetric conic and the analysis is restricted to a small field of view, so that the Seidel aberration expansion remains valid. Let the occlusion ratio of the secondary mirror to the primary mirror be denoted as α_1, the occlusion ratio of the tertiary mirror to the secondary mirror as α_2, the magnification of the primary mirror as β_1, and the magnification of the secondary mirror as β_2. The relationships between these parameters are as follows:

$$\alpha_1 = \frac{D_2}{D_1}, \alpha_2 = \frac{D_3}{D_2}, \beta_1 = \frac{l'_2}{l_2} \tag{1}$$

where l_2 and l'_2 denote the conjugate distances used in defining the corresponding magnification.

Please cite this article as: Y. Zhang, P. Guo, M. Tian et al., A High-Efficiency Off-Axis Space Solar Concentrator with Large Tolerance for Acceptance Angle Variations, Engineering, https://doi.org/10.1016/j.eng.2026.08.029

In the present design, the entrance aperture of the primary mirror D_1 is fixed to 300 mm by the thermal-power requirement of the off-axis concentrator. The diameters of the secondary and tertiary mirrors (D_2, D_3) are then determined from the baseline coaxial three-mirror layout so that the target geometric concentration ratio is achieved while the on-axis central obscuration remains within the mechanical envelope of the prototype. Once D_2 and D_3 are fixed by these optical and packaging constraints, the dimensionless ratios α_1 and α_2 are not treated as free fitting parameters, but are uniquely determined by the initial coaxial design. In the subsequent off-axis transformation and conjugate-mirror optimization, α_1 and α_2 are kept constant and serve as key inputs to the third-order aberration analysis in Eqs. (2)–(5).

According to aberration theory [31], the initial state coefficients for spherical aberration S_1, coma aberration S_2, astigmatism S_3, and field curvature S_4 of the coaxial concentrator's triple-reflector system can be calculated as follows:

$$S_1 = \frac{1}{4}\left[(e_1^2-1)\beta_1^3\beta_2^3 - e_2^2\alpha_1\beta_2^3(1+\beta_1)^3 + \alpha_1\beta_2^3(1+\beta_1)(1-\beta_1)^2\right] \tag{2}$$

$$S_2 = \frac{1}{4\beta_1}\left[-e_2^2(\alpha_1-1)(1+\beta_1)^3 + (\alpha_1-1)(1+\beta_1)(1-\beta_1)^2 - 2\beta_1\right] \tag{3}$$

$$S_3 = \frac{-e_2^2(\alpha_1-1)^2(1-\beta_1)^2 + (\alpha_1-1)^2(1+\beta_1)(1-\beta_1)^2}{4\alpha_1\beta_1^2} - \frac{(\alpha_1-1)(1+\beta_1)(1-\beta_1)}{\alpha_1\beta_1} - \beta_1 + \frac{1+\beta_1}{\alpha_1} - \frac{2}{\alpha_1\alpha_2} \tag{4}$$

$$S_4 = \beta_1 - \frac{1+\beta_1}{\alpha_1} - \frac{2}{\alpha_1\alpha_2} \tag{5}$$

where e_1 represents the aspheric coefficient of the primary mirror in the concentrator, and e_2 represents the aspheric coefficient of the secondary mirror.

At this stage, the primary, secondary, and tertiary mirrors are modeled as rotationally symmetric quadratic (conic) surfaces obtained from a coaxial three-mirror reflector. This quadratic approximation is consistent with classical third-order Seidel aberration theory, which provides closed-form expressions for $S_1 - S_4$ as functions of the occlusion ratios α_1, α_2, and the magnification β_1. These analytical coefficients characterize the baseline aberration level of the coaxial system and serve as the starting point for the subsequent off-axis freeform optimization.

The optical path design of the off-axis concentrator relies on shifting the coaxial concentrator, meaning the off-axis concentrator can be regarded as a part of the coaxial system, but with a displacement that moves the optical path from the central region to the outer periphery. In this process, a well-designed off-axis distance not only avoids central occlusion but also ensures effective light concentration, allowing the receiving surface to efficiently capture the concentrated solar energy. For accurate calculations and modeling, this study first establishes the off-axis concentrator's coordinate system, which shares the same principal optical axis as the coaxial concentrator. This provides a precise framework for describing the offset between the off-axis concentrator and the optical axis, providing flexible interfaces for subsequent optical path analysis. To better analyze the optical performance of the off-axis concentrator, this study divides the reflective surface into multiple layers. The near-axis region, close to the optical axis, is defined as the first layer. As the off-axis distance increases, the number of layers gradually rises until the outermost region reaches the N_{layer}th layer. This layered design is visually represented in Fig. 1(c), demonstrating a gradual transition from the optical axis to the edge. Each layer of the reflective surface has different optical characteristics due to variations in position and angle, making it necessary to model the optical path for each layer separately to ensure accurate parameter corrections.

2.2. Geometric construction method for the concentrator reflective surface

Based on the D–H matrix transformation and the principle of skew ray vector transmission [32], the exact calculation of discrete points is ensured during the generation of transition arcs between two discrete points [33]. The solution process is illustrated in Fig. 1(d), and the specific steps are as follows [34]:

(1) A ray $\boldsymbol{v}_{s,0}$ is emitted from the initial point $\boldsymbol{P}_{s,0}$, and this ray intersects with the concentrator reflective surface at point $\boldsymbol{P}_0$. Based on the target point position on the receiving surface and the relative position of the concentrator, the target vector $\boldsymbol{v}_{t,0}$ and target point $\boldsymbol{P}_{t,0}$ are determined. The normal at the intersection between the incident ray and the concentrator surface is then calculated:

$$n_0 = \frac{v_{t,0}}{|v_{t,0}|} - \frac{v_{s,0}}{|v_{s,0}|} \tag{6}$$

$$\boldsymbol{v}_0 = \boldsymbol{P}_0 + \boldsymbol{n}_0 t_0 \tag{7}$$

where $\boldsymbol{n}_0$ is the normal vector at the intersection point, $\boldsymbol{v}_0$ represents the matrix of the extended normal line, and t_0 represents the angular amplitude.

(2) A ray $\boldsymbol{v}_{s,1}$ is emitted from the second point $\boldsymbol{P}_{s,1}$ toward the concentrator's reflective surface, and it is required to reflect the ray to the target point $\boldsymbol{P}_{t,1}$. Therefore, a scalar $[P_{s,1}, v_{s,1}]^{\mathrm{T}}$ exists, which can express the intersection point $\boldsymbol{P}_1$ through the incident ray as follows:

$$\boldsymbol{P}_1 = \boldsymbol{P}_{s,1} + \lambda_{s,1}\boldsymbol{v}_{s,1} \tag{8}$$

Since the reflective surface of the concentrator is adjusted based on a spherical surface, the initial state of $\widehat{P_0P_1}$ assumed in this study is a circular arc-shape. The normal vectors $\boldsymbol{n}_o$ and $\boldsymbol{n}_1$ are both perpendicular to the respective positions on the arc. Therefore, the following relationship exists:

$$\overline{C_0P_0} = \overline{C_0P_1} \tag{9}$$

where C_0 denotes the center of the circular arc passing through P_0 and P_1. Point P_0 is a known value, and the position vector of point P_1 (denoted by P_1) can be calculated as follows:

$$\boldsymbol{P}_1 = \boldsymbol{v}_1 - \boldsymbol{n}_1\boldsymbol{t}_1 \tag{10}$$

By expressing the extended normal line as a single-valued function of the angular amplitude, the normal vector $\boldsymbol{n}_1$ can be calculated as:

$$\boldsymbol{n}_1 = \mathbf{Rot}(y,\theta_1)(-\boldsymbol{v}_{s,1}) \tag{11}$$

$$\boldsymbol{v}_i = \boldsymbol{P}_i + \boldsymbol{n}_i\boldsymbol{t}_i (i = 1,2,\ldots,n) \tag{12}$$

$$\theta_1 = \frac{1}{2}\cos^{-1}(-\boldsymbol{v}_{s,1}\cdot\boldsymbol{v}_{t,1}) \tag{13}$$

where **Rot** denotes the homogeneous-coordinate rotation transformation matrix; θ_1 is half of the angle between $v_{s,1}$ and $v_{t,1}$; i denotes the index of the discrete construction point on the reflective surface, and n denotes the total number of discrete construction points along the surface profile.

(4) By substituting the solved $\lambda_{s,1}$ into Eqs. (10) and (11), the coordinates of point $\boldsymbol{P}_1$ and the normal vector $\boldsymbol{n}_1$ can be obtained. Then, the coordinates and normal vectors of points $\boldsymbol{P}_2, \boldsymbol{P}_3, \ldots, \boldsymbol{P}_n$ are

Please cite this article as: Y. Zhang, P. Guo, M. Tian et al., A High-Efficiency Off-Axis Space Solar Concentrator with Large Tolerance for Acceptance Angle Variations, Engineering, https://doi.org/10.1016/j.eng.2026.08.029

calculated in sequence. By connecting all the points and applying arc transitions between them, the complete surface profile of the concentrator's reflective surface can be constructed.

2.3. Feedback iterative optimization

When modeling the concentrator's reflective surface using the geometric construction method, the solar divergence angle affects the normal vectors at each intersection point, making it difficult to ensure their accuracy. Therefore, this study adopts a feedback iterative optimization method to compensate for and optimize the normal vectors of the intersection points formed under different incident angles, adjusting the radiation transmission path during reflection. By neglecting energy loss in the reflection process, the concentrator's role is limited to regulating the distribution of energy transmission. Thus, in an ideal scenario, the total radiation energy incident on the concentrator equals the total radiation energy received by the receiving surface. Based on the law of energy conservation, the following relationship holds:

$$\iint_{D_1} I(\theta_1, r_1)\mathrm{d}\theta\mathrm{d}r = \iint_{D_E} E(\theta_E, r_E)\mathrm{d}\theta\mathrm{d}r \tag{14}$$

where (θ, r) represents the polar coordinates of the discrete points, I represents the solar irradiance (taken as 1361 $\mathrm{W{\cdot}m^{-2}}$), E represents the irradiance received by the receiving surface ($\mathrm{W{\cdot}m^{-2}}$).

The target feedback energy flux on the receiving surface is defined as:

$$Ef_k(\varphi, r) = \prod_{i=1}^{k} \beta_i(\varphi, r) \cdot E_0(\varphi, r) \tag{15}$$

where $E_0(\varphi, r)$ is the irradiance received by the receiving surface, $E_k(\varphi, r)$ is the irradiance received by the receiving surface after the kth iteration, $\beta_i(\varphi, r)$ is the feedback iteration coefficient, $Ef_k(\varphi, r)$ is the target feedback energy flux.

The feedback coefficient β_k is given by:

$$\beta_k(\varphi, r) = \{E_0(\varphi, r)/[\lambda_1 \cdot E(\varphi, r) + (1 - \lambda_1) \cdot E_0(\varphi, r)]\}^{\lambda_2} \tag{16}$$

By combining the geometric construction method with the Monte Carlo ray tracing (MCRT) simulation, the discrete irradiance distribution on the receiving surface is updated iteratively, and the surface-shape coefficients are adjusted until the evaluation function becomes sufficiently small. The merit function is defined as:

$$\mathrm{MF} = \sqrt{\frac{\sum_{p=0}^{N_r}\sum_{q=0}^{N_d}\left(\frac{E_k(\varphi_q, r_p) - E_0(\varphi_q, r_p)}{E_0(\varphi_q, r_p)}\right)^2}{(N_r + 1)(N_d + 1) - 1}} \tag{17}$$

where MF denotes the merit function for evaluating the irradiance distribution error, N_r represents the number of radial grid divisions, N_d represents the number of circumferential grid divisions, p and q represent the radial and circumferential grid indices, respectively. After multiple iterations and adjustments of the coefficients, when the evaluation function reaches its minimum value, the optimal solution for the concentrator's reflective surface shape adjustment is achieved.

In the optimization process, convergence is deemed to be reached when MF falls below 5×10^{-3} and the relative change of MF between two successive iterations is less than 1%. For the final design covering an acceptance half-angle of ±0.5°, the feedback optimization typically required 100–500 iterations, with 1×10^5 rays traced in each iteration. On a standard workstation (Intel i7 CPU, 3.0 GHz, 32 GB RAM), the computation time for a single optimization adjustment is approximately 30 min. Under these settings, the minimum value of the evaluation function is on the order of $\mathrm{MF_{min}} \approx 3 \times 10^{-3}$ at normal incidence and remains below 8×10^{-3} at the edge of the design field, indicating that the optimized irradiance distribution closely follows the prescribed target profile.

3. Optimization simulation

Concentration uniformity is one of the core metrics used for evaluating the optical performance of a concentrator, as it directly determines the energy conversion efficiency of the receiving surface. In practical applications, uniformity is typically assessed based on the evenness of the irradiance distribution across the focal plane. The more uniform the distribution, the higher the energy utilization efficiency and the lower the risk of thermal stress. To achieve a quantitative evaluation, this study first employs the standard deviation of irradiance within the focal spot to capture the intensity fluctuations. However, a single standard deviation measure is highly sensitive to local anomalies and cannot fully represent overall uniformity. To mitigate possible misinterpretation caused by edge irradiance decay, the evaluation function incorporates the maximum irradiance of the focal spot, using a weighted correction to enhance the representation of the overall focal structure. The final uniformity metric is formulated as follows [34]:

$$\sigma_\mathrm{I} = \sqrt{\frac{1}{m}\sum_{j=1}^{m}\left(I_\mathrm{rec}(x_j, y_j) - I_\mathrm{avg}\right)^2} \tag{18}$$

$$U = \max\left\{0,\ 1 - \frac{\sigma_\mathrm{I}}{I_\mathrm{max} - I_\mathrm{avg}}\right\} \tag{19}$$

where σ_I denotes the standard deviation of irradiance within the focal spot region, $I_\mathrm{rec}(x_j,\ y_j)$ represents the irradiance collected on the receiving surface during the jth sampling, m is the total number of samples, I_avg is the average irradiance of the focal spot region, I_max is the maximum irradiance within the focal spot region, U represents the concentration uniformity.

The RMS spot radius R_RMS denotes the irradiance-weighted root-mean-square distance of the focal-spot energy distribution from its centroid on this plane, defined as [34]:

$$R_\mathrm{RMS} = \sqrt{\frac{\sum_{j=1}^{m} w_j\left(\left(x_j - x_\mathrm{c}\right)^2 + \left(y_j - y_\mathrm{c}\right)^2\right)}{\sum_{j=1}^{m} w_j}} \tag{20}$$

where ω_j is the irradiance weight at the jth sampling point, and $(x_\mathrm{c},\ y_\mathrm{c})$ is the energy centroid.

3.1. Analysis of off-axis spot variation trends

Using the MCRT method, a preliminary study of the angular response of the off-axis concentrator was conducted within a small-angle comprehensive field of view. Representative point plots and irradiance distributions at selected incidence angles are shown in Fig. 2, while the corresponding overall angular-response characteristics are summarized in Fig. 3(a).

In this model, tracking errors of the solar tracker are represented as small rotations of the incident beam about the X- and Y-axes, denoted by θ_x and θ_y, respectively. Let s_0 be the nominal incident direction vector. The perturbed incident direction $s(\theta_x,\ \theta_y)$ is expressed as:

$$\boldsymbol{s}(\theta_x, \theta_y) = \boldsymbol{R}_x(\theta_x)\boldsymbol{R}_y(\theta_y)\boldsymbol{s}_0 \tag{21}$$

Please cite this article as: Y. Zhang, P. Guo, M. Tian et al., A High-Efficiency Off-Axis Space Solar Concentrator with Large Tolerance for Acceptance Angle Variations, Engineering, https://doi.org/10.1016/j.eng.2026.08.029

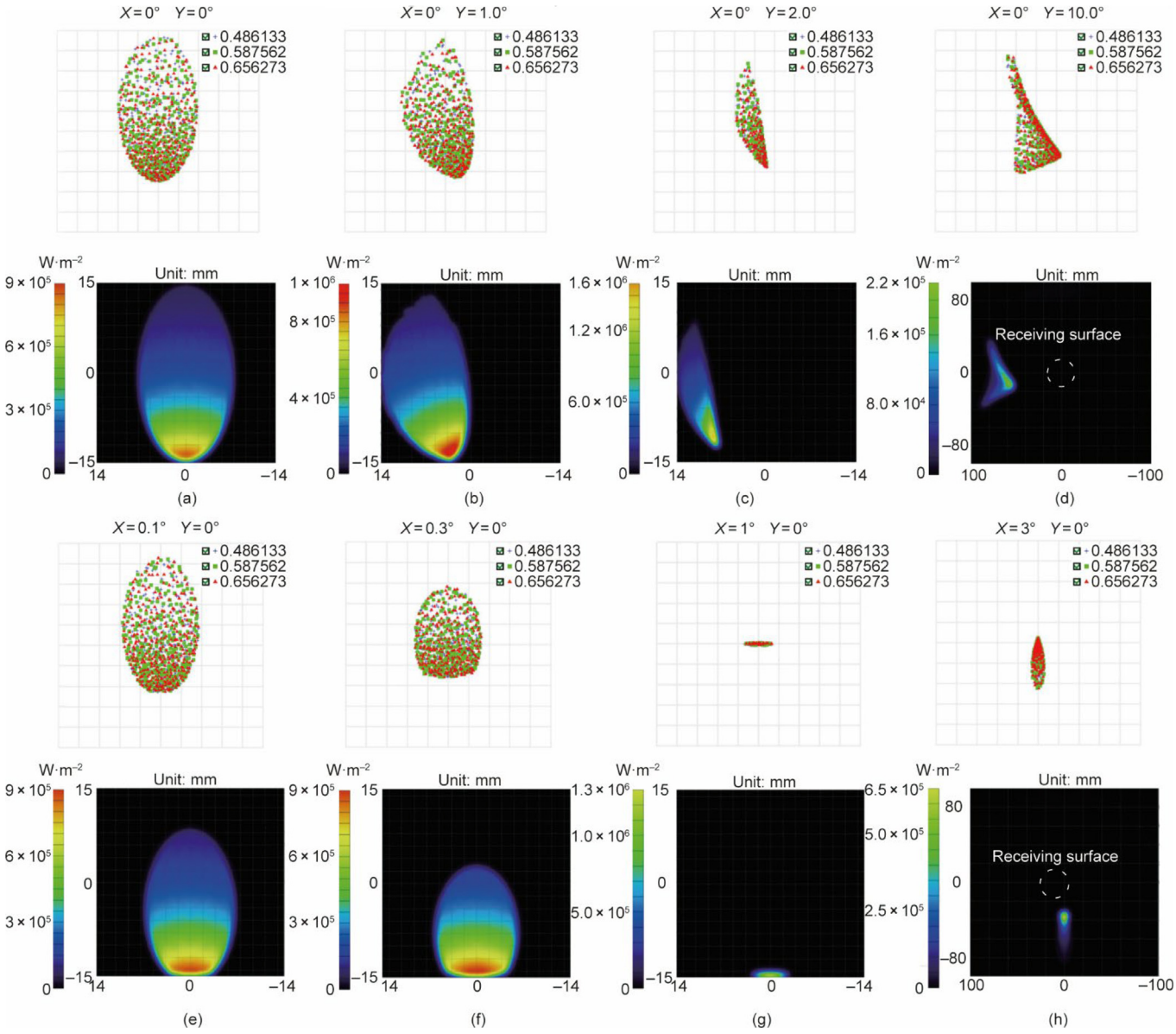


Fig. 2. Point plot and irradiance map of the off-axis concentrator at various incidence angles along the *Y*- and *X*- axes: (a) normal incidence, (b) incident light rotated by 1.0° around the *Y*-axis, (c) incident light rotated by 2.0° around the *Y*-axis, (d) incident light rotated by 10.0° around the *Y*-axis, (e) incident light rotated by 0.1° around the *X*-axis, (f) incident light rotated by 0.3° around the *X*-axis, (g) incident light rotated by 1.0° around the *X*-axis, (h) incident light rotated by 3.0° around the *X*-axis.

where R_x and R_y are the rotation matrices around the *X*- and *Y*-axes. By varying θ_x and θ_y within a small range, the resulting angular response directly reflects the concentrator's sensitivity to tracking inaccuracies.

When light is incident perpendicular to the concentrator, all rays are concentrated on the receiving surface, as shown in Fig. 2(a). This indicates that under ideal incident conditions, without considering the effects of mirror reflectivity and errors, the concentrator's concentration efficiency can nearly reach 90%, with a concentration ratio exceeding 100. The irradiance energy of the focal spot exhibits a bell-shaped distribution with a peak near the center, with the energy flux density being highest at the center and gradually decreasing towards the edges. Due to the off-axis nature of the concentrator, the light rays are shifted during the concentration process, resulting in an elliptical focal spot with an irradiance peak near the bottom edge under normal incidence. When the incident angle rotates by 1.0° around the *Y*-axis, as shown in Fig. 2(b), most of the light rays can still be concentrated onto the receiving surface, but the energy flux distribution becomes uneven. Ninety percent of the energy is concentrated on 70% of the area, causing local deformation of the focal spot, with some regions showing irradiance peaks even higher than those under normal incidence. As shown in Fig. 2(c), when the rotation angle reaches 2.0°, the concentration efficiency drops sharply to 38.9%. When the rotation angle exceeds 2.5°, none of the rays reflected by the off-axis primary mirror can reach the receiving surface. From the spot shape changes in Figs. 2(a)–(c), it can be observed that since the incident light rotates along the *Y*-axis, the focal spot slowly migrates along the *X*-axis. Additionally, because the off-axis concentrator is eccentric along the *Y*-axis, the focal spot shape tends to be compressed along the *Y*-axis. Analyzing the changes in the effective concentrating area shows that small-angle rotation of the incident light causes the focal spot to resemble a candle flame being blown. When the rotation angle of the incident light is large enough, as shown in Fig. 2(d), the focal spot completely deviates from the receiving surface, further intensifying its deformation.

Please cite this article as: Y. Zhang, P. Guo, M. Tian et al., A High-Efficiency Off-Axis Space Solar Concentrator with Large Tolerance for Acceptance Angle Variations, Engineering, https://doi.org/10.1016/j.eng.2026.08.029

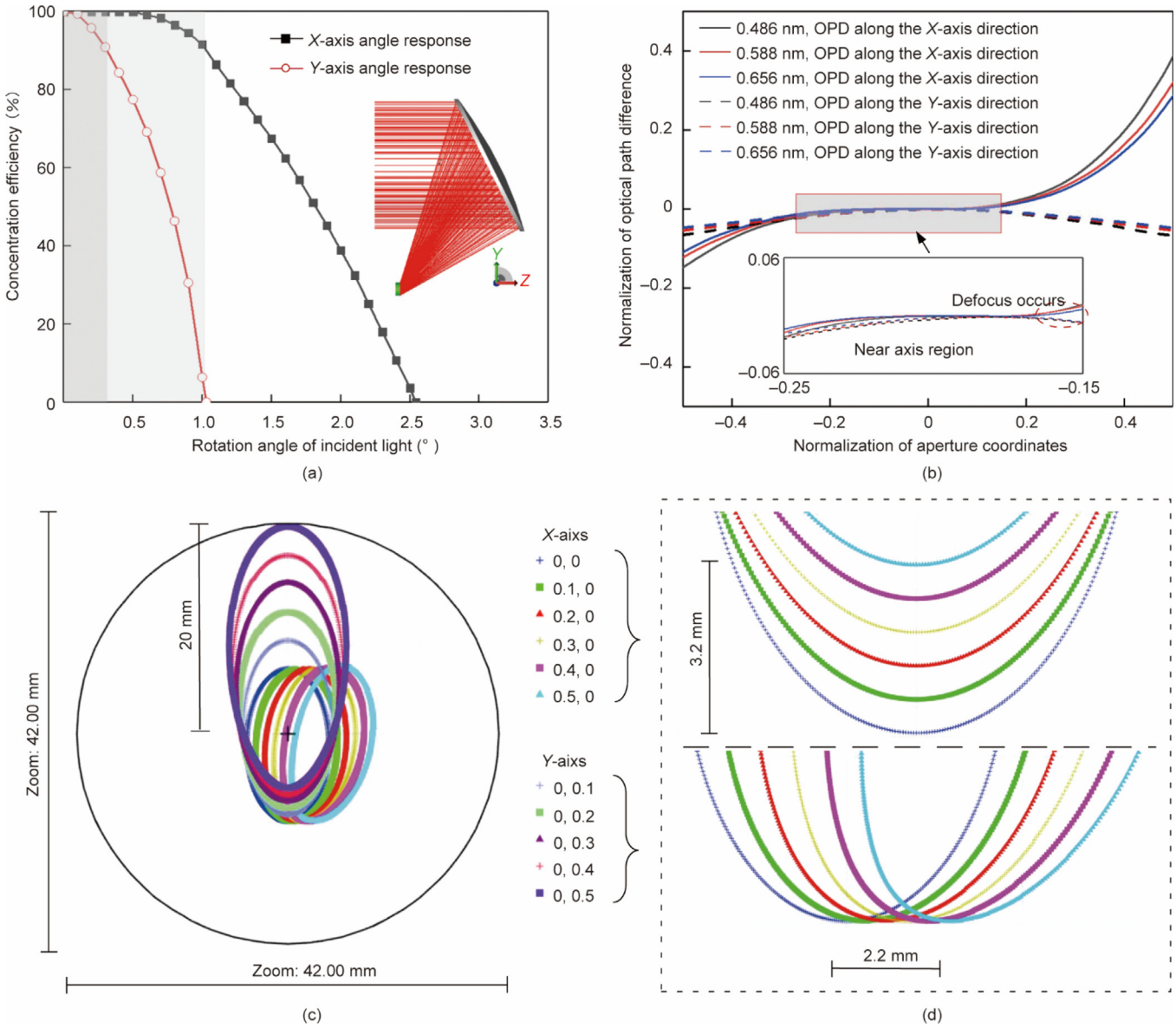


Fig. 3. Comprehensive analysis of angular response: (a) angular response characteristic curve of the off-axis concentrator; (b) optical path difference diagram of the meridional/sagittal plane; (c) ray-trace diagram at different incident angles with the relative position of the central point unchanged; (d) enlarged spot shift diagram for *X*- and *Y*-axis response.

Thus, it can be concluded that when the incident light rotates along the *Y*-axis, the primary factor affecting concentration efficiency is the deformation of the focal spot, followed by the offset of the focus.

The incident irradiance in the simulation is set to 1361 $W \cdot m^{-2}$, corresponding to the air-mass-zero (AM0) solar constant. Optimization tuning and surface-shape generation are performed using Ansys Zemax OpticStudio software, while MCRT simulations are carried out in TracePro. The Sun is modeled as a collimated source using three representative Fraunhofer F, d, and c spectral lines at wavelengths of 0.486, 0.588, and 0.656 μm, respectively, with mirror reflectance $\rho = 0.90$ and uniform irradiance over the 300-mm aperture of the primary mirror. This configuration is equivalent to an ideal parallel-beam sunshape without an explicit finite solar disk. The finite solar angular divergence (≈0.27° half-angle) is smaller than the designed acceptance half-angle (±0.5°); therefore the collimated-beam approximation is adopted, and the detailed sunshape has only a secondary influence on the geometric concentration compared with aberrations and tracking errors. For each incidence angle, 1×10^5 rays are launched per configuration using TracePro's built-in random ray generator with uniform sampling over the source aperture. A ray-count convergence test was performed by increasing the number of rays from 5×10^4 to 2×10^5; once the ray counts exceeded 1×10^5, the variations in the effective concentration ratio and in the root mean square (RMS) radius on the receiving surface were below 3%. Therefore, 1×10^5 rays are adopted for all parametric studies as a compromise between accuracy and computational cost, whereas 5×10^5 rays are used for the final design verification and slope-error sensitivity analysis. For clarity in visualizing the energy distribution, only 20 representative rays are shown in the spot plots.

Simulating the angular response of the off-axis concentrator along the *X*-axis (Fig. 2(e)), when the incident light rotates by 0.1°, the entire spot shifts downward. As the rotation angle increases to 0.3°, the concentration efficiency decreases to 90.9%. At a 1.0° rotation, almost no rays reach the receiving surface, and

Please cite this article as: Y. Zhang, P. Guo, M. Tian et al., A High-Efficiency Off-Axis Space Solar Concentrator with Large Tolerance for Acceptance Angle Variations, Engineering, https://doi.org/10.1016/j.eng.2026.08.029

the concentration efficiency drops to just 6.4%. By analyzing the irradiance values and spot shape changes in Figs. 2(e)–(g), it is observed that as the rotation angle around the *X*-axis increases, the overall shape of the spot retains its initial elliptical form, with only localized deformation. Moreover, this deformation does not cause the spot to deviate from the receiving surface, indicating that spot deformation is not the main factor affecting concentration efficiency along the *X*-axis. Since the initial structure of the off-axis concentrator is eccentric along the *Y*-axis, when the incident light rotates around the *X*-axis, the spot rapidly shifts along the *Y*-axis, causing the spot to shift downward until it moves off the receiving surface. From the irradiance maps, it is clear that the offset of the focus has a more significant impact on concentration efficiency than deformation, which contrasts with the conclusions drawn from the *Y*-axis angular response. However, by combining the reflection ray aggregation process from the point plots, it is evident that both the energy concentration position and spot shape are changing. When the rotation angle continues to increase, as seen in Fig. 2(h), the spot undergoes large-scale reverse deformation. This suggests that the analysis of spot shape changes in Figs. 2(e)–(g) is incomplete, as the spot may undergo regular, large-scale changes and be compressed until reverse stretching occurs, as seen in Fig. 2(h). Therefore, this study hypothesizes that when the incident light rotates around the *X*-axis, the main factor affecting concentration efficiency is spot deformation, followed by the offset of the focus. This indicates that the off-axis concentrator's angular response along the *X*- and *Y*-axes exhibits the same trend, with similar factors influencing concentration efficiency.

In Fig. 3(a), the variation in concentration efficiency in response to *X*- and *Y*-axis rotations is shown more clearly. When the incident light rotates at small angles, such as less than 0.1°, the angular responses of both the *X*- and *Y*-axis maintain the concentration efficiency at over 99%. However, as the rotation angle increases, both *X*- and *Y*-axis angular responses show an accelerated decline in concentration efficiency, reflected by the increasing slope of the curves, with different trends of decline for each axis. Quantitatively, when the tracking errors remain within $|\theta_x| \leq 0.5°$ and $|\theta_y| \leq 0.5°$, the concentration efficiency remains about 78% of the on-axis value, and the RMS radius of the focal spot increases by less than approximately 20%. For larger tracking errors in the range of 1°–2°, the concentration efficiency decreases more rapidly and the focal spot becomes strongly distorted, indicating the practical tolerance range for the proposed off-axis concentrator.

To analyze the aberrations leading to spot deformation and the trend of spot displacement, the position of the spot on the focal plane was simulated in Zemax under different rotation angles, with ray tracing performed. Fig. 3(b) shows the normalized optical path difference (OPD) along the *X*- and *Y*-axis directions at the three representative wavelengths. The near-axis region exhibits relatively stable OPD variations, whereas larger deviations occur toward the aperture edges, indicating increased aberration away from the near-axis region. As shown in Fig. 3(c), during the *X*-axis response process, it can be concluded that coma aberration and spherical aberration are the primary factors causing spot deformation. Coma aberration not only elongates the spot along the *Y*-axis during the *X*-axis response but also causes the spot to rotate around the focal point during the *Y*-axis response. Fig. 3(d) shows that the spot displacement varies in a consistent, gradual increase without sudden jumps, and the displacement does not affect the spot size. This further confirms the conclusions drawn from Fig. 2, namely that when the incident light rotates along the *X*- or *Y*-axis, the primary factor contributing to the loss of concentration efficiency is spot deformation, while spot displacement has a relatively minor impact.

By combining the spot edge deformation trends in Figs. 3(c) and (d), the phenomenon that the *X*-axis angular response declines much faster than the *Y*-axis angular response can be explained. This occurs because the off-axis concentrator's eccentricity along the *Y*-axis causes the spot shape to deform, leading to a larger portion of the spot deviating from the receiving surface, which results in a loss of concentration efficiency. In Fig. 3(b), the middle region of the curve corresponds to the near-axis section, where changes remain within a stable fluctuation range. The variations on both sides of the curve explain the underlying cause of the spot edge curve changes in Fig. 3(c), namely, coma aberration and spherical aberration, which cause some rays in the main optical path to deflect. This leads to a large-scale shift of the spot in the direction of the incident light's rotation angle. Therefore, to control the spot shape, eliminating aberrations in the off-axis concentrator is the most effective way to improve concentration efficiency.

3.2. Off-axis conjugate focusing method

Considering the influence of the Sun's divergence angle, the acceptance angle of the off-axis concentrator needs to be increased. Therefore, a small-angle field of view optimization was performed for the off-axis concentrator based on spherical mirrors. In prior outdoor concentration experiments with dish concentrators, a significant phenomenon was observed: As the dish depth decreased, the impact of surface shape and assembly errors on concentration performance increased significantly, especially highlighting the differences in concentration performance between the near-axis and edge regions [35]. This finding indicates that shallower dish designs make the concentrator more susceptible to error interference in practical applications, leading to reduced concentration efficiency and degraded spot quality. To address this issue, it is essential to control interference factors before optimization by increasing the dish depth, thereby enhancing the concentrator's adaptability to complex environments. Specifically, this study constrained the focal-to-diameter ratio of the off-axis concentrator between 1 and 1.5 to ensure that, even with increased dish depth, the concentrator can maintain an effective acceptance angle. However, this design choice introduced new challenges. Due to the small focal-to-diameter ratio, the rays reflected from the edge regions of the off-axis concentrator gradually converge toward the near-axis area, and in some cases, overlapping of reflected rays occurred. This overlap and crossing of optical paths not only increased the complexity of the internal optical path but also directly affected the overall concentration efficiency of the concentrator, as shown in Fig. 4(a).

In the preliminary optimization process, the position of the focal plane was adjusted to initially refine the shape of the spot on the receiving surface. The results showed that as the focal plane's forward distance increased, the spot shape on the receiving surface gradually transitioned from an initial flattened elliptical shape to a longer elliptical form. However, as the distance continued to increase, the off-axis concentrator soon reached its concentration ratio limit, and the resulting spot took on a T-shaped overlay pattern. The appearance of this concentration ratio limit indicated that further optimization would only lead to minor changes in the spot shape, with no significant improvements. Moreover, the concentration ratio limit only reached 200, much lower than the theoretical maximum, indicating that the spherical aberration produced by the off-axis concentrator in the current design could not be ignored. The presence of spherical aberration caused rays to deviate from the ideal focal point, worsening as the rays moved farther from the optical axis, significantly impairing the system's concentration performance.

Please cite this article as: Y. Zhang, P. Guo, M. Tian et al., A High-Efficiency Off-Axis Space Solar Concentrator with Large Tolerance for Acceptance Angle Variations, Engineering, https://doi.org/10.1016/j.eng.2026.08.029

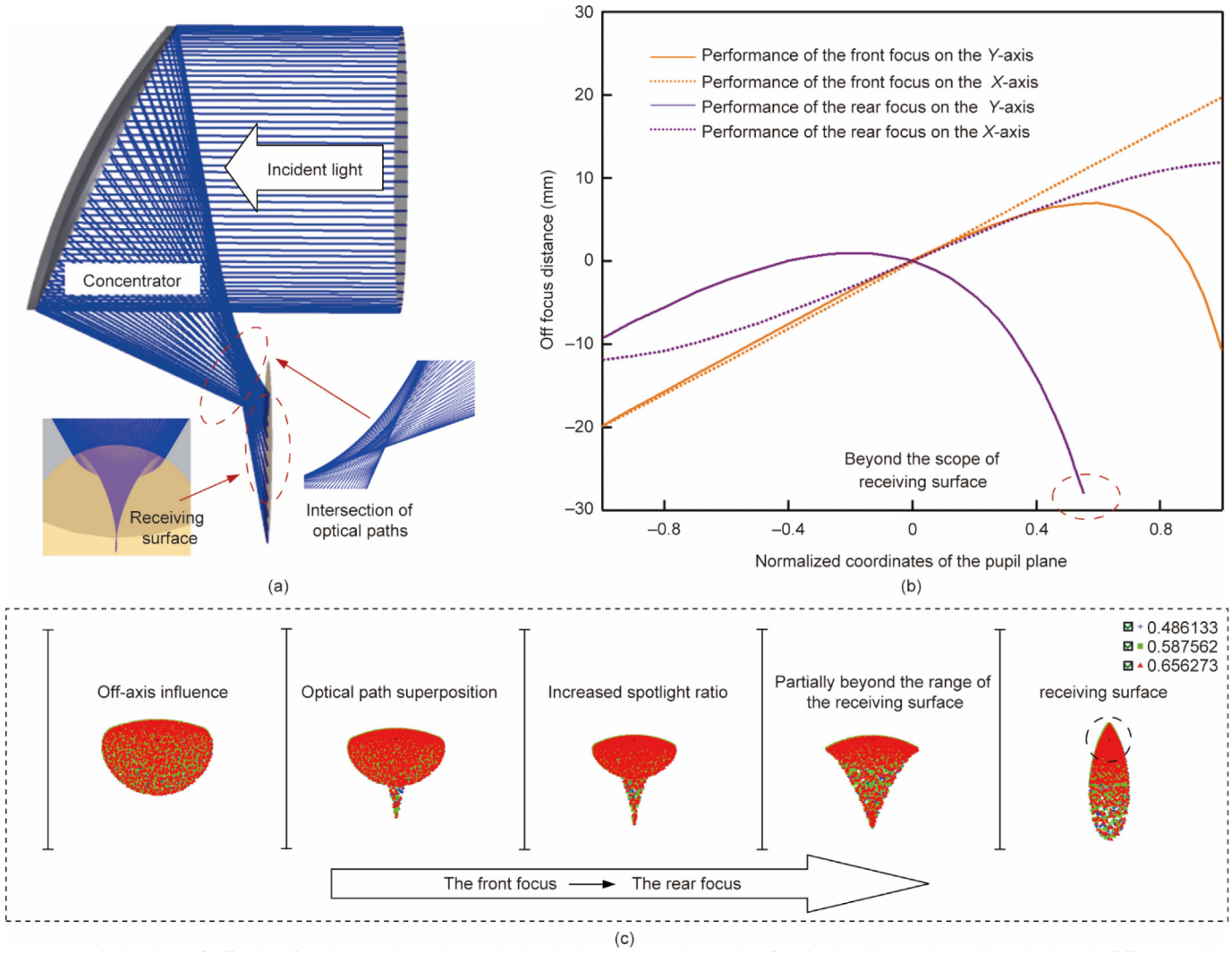


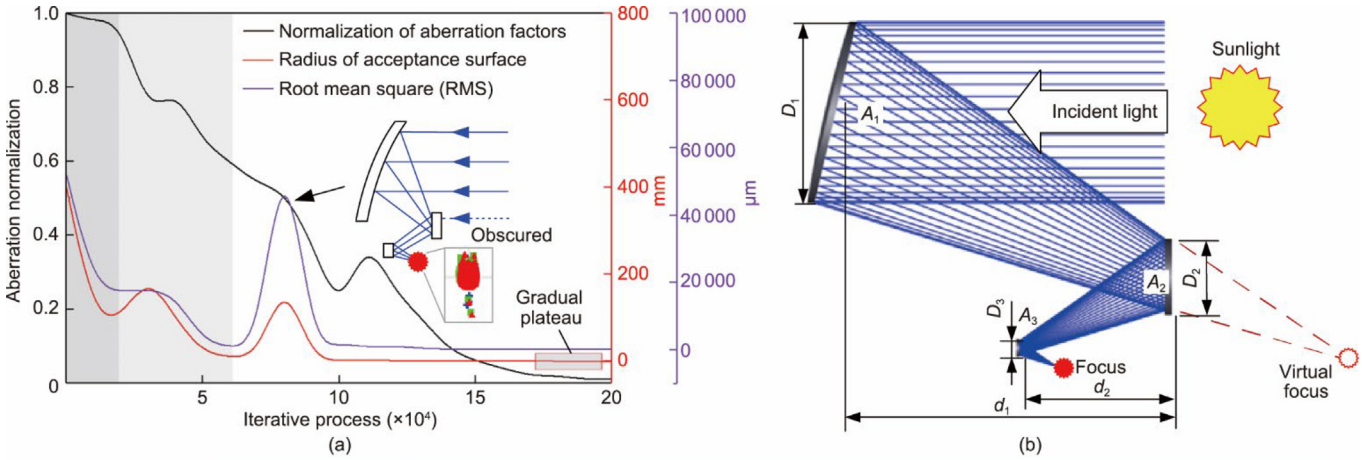
Fig. 4. Optimization of effective focal power based on spherical mirrors: (a) schematic of optical path crossing; (b) optical path difference diagram; (c) changes in the point plot during the focusing process.

Although the focal-spot area is reduced during the focusing process, the optical path difference shown in Fig. 4(b) indicates that the defocusing of the edge rays is not effectively mitigated. As the focal plane was gradually moved backward, the spot shape was further elongated (Fig. 4(c)), and the expanding spot area led to an increasing receiving surface radius, which in turn caused a blocking effect on the off-axis concentrator. This occlusion not only limited the effective acceptance area of the concentrator but also led to a severe decline in concentration efficiency, further degrading the overall system performance. To solve this issue, the study performed fine adjustments in the $0 < x < 2$ optimization range in Fig. 5(a), using an effective focal power-weighted adjustment to reposition the receiving surface. This resulted in an optimal surface shape parameter that could effectively reflect light. This optimization process ensured that light reflection in various regions was properly corrected, laying the foundation for subsequent spot shape adjustments and aberration compensation.

The variation of the focal-plane position can be regarded as a defocus-type error, which may arise from thermoelastic deformation or structural settling of the receiving surface support. During the focusing process of the off-axis concentrator, although the spot area was minimized through focusing, the issue of uncontrolled spot shape persisted. Specifically, the defocusing of edge rays was not effectively mitigated (Fig. 4(b)), and the edge of the T-shaped spot showed noticeable warping and deformation. This deformation not only makes efficient use of solar energy more challenging but also negatively impacts the overall concentration efficiency of the concentrator. Considering subsequent assembly and tracking errors, if the receiving surface deviates by 2 mm from the ideal focal plane, the RMS radius will increase significantly, reaching millimeter-level values. Such an increase in error would severely impair the system's concentration performance. If the receiving surface deviates by 10 mm from the ideal focal plane, the spot shape will evolve into a long, narrow elliptical form, as shown in Fig. 4(c). At this point, a large portion of the spot will extend beyond the receiving surface, causing the concentration efficiency to drop sharply, to below 50%. This poses a serious threat to the system's overall performance, especially in applications requiring high-precision solar energy concentration.

To further improve the concentration ratio, the issue of optical path crossing must be addressed. For this reason, the surface shape of the off-axis concentrator was adjusted based on freeform surfaces. The specific approach involved referencing an RMS-based optimization function related to centroid settings and then

Please cite this article as: Y. Zhang, P. Guo, M. Tian et al., A High-Efficiency Off-Axis Space Solar Concentrator with Large Tolerance for Acceptance Angle Variations, Engineering, https://doi.org/10.1016/j.eng.2026.08.029



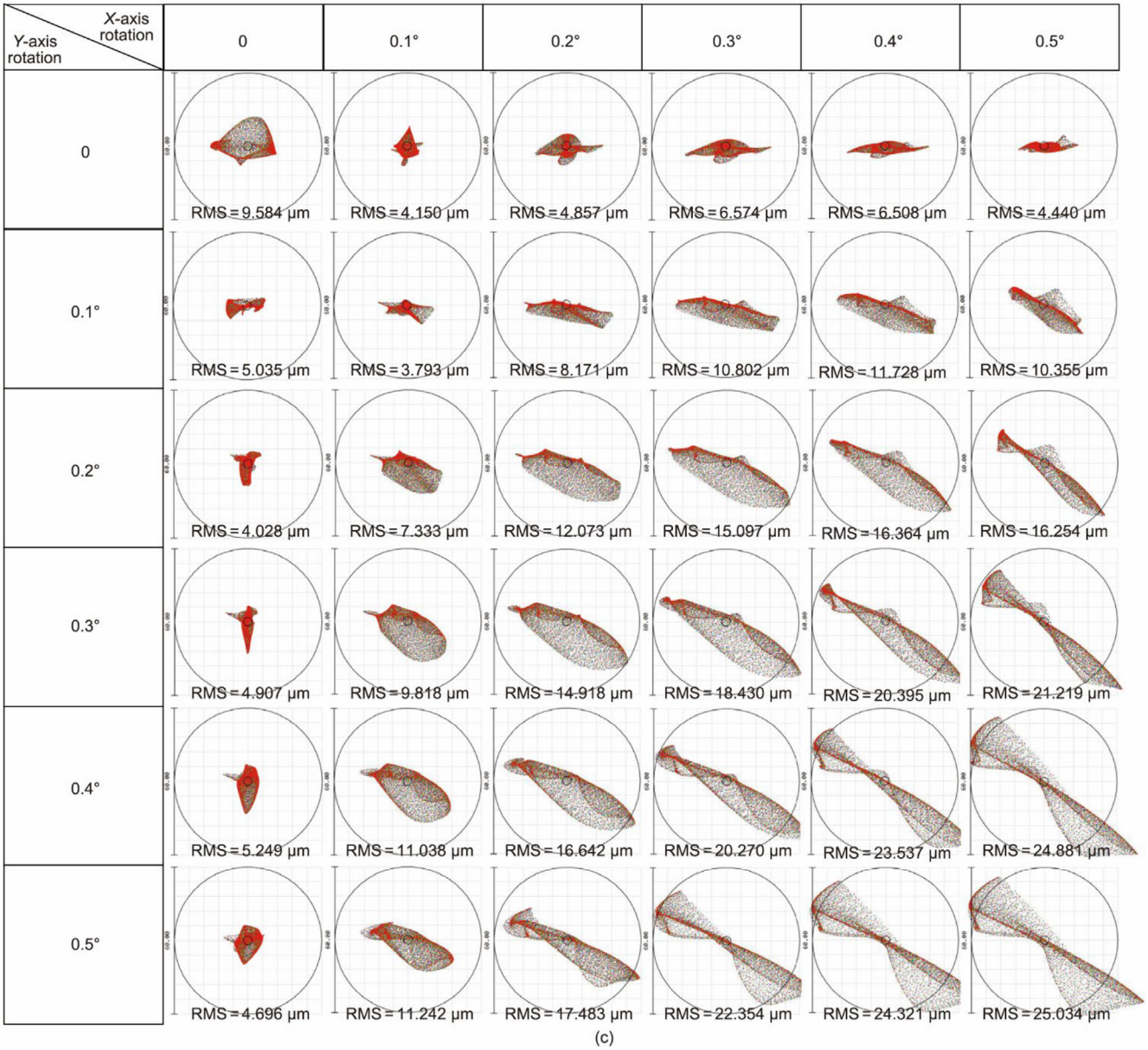


Fig. 5. Optimization iteration process: (a) changes in aberration coefficient, receiving surface radius, and RMS value during optimization process; (b) off-axis conjugate triple-reflector optical path; (c) optimized point array diagram of focal plane in different fields of view.

Please cite this article as: Y. Zhang, P. Guo, M. Tian et al., A High-Efficiency Off-Axis Space Solar Concentrator with Large Tolerance for Acceptance Angle Variations, Engineering, https://doi.org/10.1016/j.eng.2026.08.029

optimizing accordingly. After optimization, in the $2 < x < 6$ optimization range shown in Fig. 5(a), the RMS values demonstrated a stable decrease, indicating that system errors were effectively controlled. Additionally, the fluctuations in the receiving surface radius during the optimization process had little impact on aberrations, keeping the spot deformation within controllable limits.

Considering the differences between the edge and near-axis regions of the reflective surface, as well as the newly generated higher-order aberrations during the previous optimization process, compensation for the aberrations caused by the off-axis concentrator is required, along with constraints on the spot's edge area. To achieve this, a conjugate mirror was introduced between the off-axis concentrator and the focal point. This design introduces a secondary reflection path into the main optical path, and by optimizing the surface shape of the conjugate mirror, it specifically compensates for higher-order aberrations while providing additional control parameters for the spot shape. The optimization process primarily focuses on the changes in RMS values and aberrations within the optimization range $x > 6$. The resulting off-axis conjugate triple-reflector optical path is shown in Fig. 5(b). Results indicate that the secondary focusing function of the conjugate mirror not only significantly reduces the area of receiving surface but also enhances the overall concentration ratio of the concentrator (Fig. 5(c)), while effectively compensating for the aberrations generated by the off-axis concentrator.

However, near $x = 8$, the curve shows a sharp rise and fall, indicating that adjustments to the conjugate mirror's diameter at this point cause partial occlusion of the off-axis concentrator, leading to higher-order aberrations (the inset in Fig. 5(a) sketches this occlusion geometry). These aberrations are primarily composed of coma aberration and spherical aberration, with coma aberration accounting for more than 80% of the total aberration. This results in strong fluctuations at the edge positions of the optical path, causing some rays to diffuse during transmission, which is reflected in the point plot as tail stretching that deviates from the ideal receiving surface. This deviation leads to a reduction in concentration efficiency and negatively impacts the quality of the spot. Therefore, in further optimization, the position and radius parameters of the conjugate mirror must be strictly constrained to ensure no interference between the off-axis concentrator and the conjugate mirror. By precisely adjusting these parameters, the generation of coma and the diffusion of rays can be avoided, thus maintaining the system's high concentration efficiency and spot quality.

The point plot of the optimized concentrator is shown in Fig. 5(c). The robustness of the concentrator within an acceptance half-angle of ±0.5° has been effectively enhanced. The RMS radius of the focal spot on the receiving surface in the main field of view is less than 10 μm, and the RMS radius of the full field of view is less than 26 μm. Geometrical ray-tracing results further show that, within this ±0.5° acceptance half-angle, all reflected rays are tightly confined to the effective focusing area on the receiving surface, indicating that high-order aberrations have been effectively suppressed. By adjusting the positions of the flat mirror and the receiving surface, the focal plane can be shifted, and the energy flow distribution can be homogenized (Fig. 6).

3.3. Sensitivity of optical performance to mirror slope errors

To further assess the robustness of the off-axis conjugate concentrator under realistic space conditions, mirror figure errors were introduced into the MCRT model in the form of random slope errors. Let n_{id} denote the ideal surface normal at each ray–mirror intersection. Mirror deformation is represented by a small perturbation δn with zero mean and a prescribed RMS slope error σ_s. The perturbed normal n_{pert} is given by:

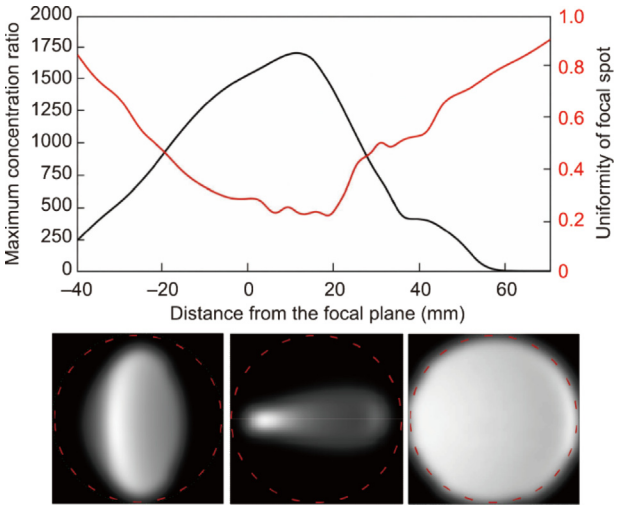


Fig. 6. Analysis of the effect of defocus distance. (a) Variation of the concentration ratio and concentration uniformity (Eq. (19)) during the process from front defocus to rear defocus; (b) variation of the focal spot shape during the process from front defocus to rear defocus.

$$\delta n \sim \mathcal{N}\left(0, \sigma_s^2 \boldsymbol{I}\right) \tag{22}$$

$$\boldsymbol{n}_{pert} = \frac{\boldsymbol{n}_{id} + \delta \boldsymbol{n}}{\| \boldsymbol{n}_{id} + \delta \boldsymbol{n} \|} \tag{23}$$

The reflected ray direction is then updated according to

$$\boldsymbol{v}_t = \boldsymbol{v}_s - 2\left(\boldsymbol{v}_s \cdot \boldsymbol{n}_{pert}\right)\boldsymbol{n}_{pert} \tag{24}$$

In this way, the combined effects of manufacturing errors, alignment imperfections and thermoelastic deformations are incorporated into the optical model through a single engineering parameter σ_s. Simulations were performed for a series of RMS slope errors σ_s = 0–3 mrad, which cover the typical range reported for high-quality solar-concentrator mirrors. For each value of σ_s, the optical concentration ratio, the RMS radius of the focal spot, and the on-axis optical efficiency on the receiving surface were calculated and normalized with respect to the ideal case. This treatment provides an engineering-equivalent way to account for net angular perturbations of surface normals, rather than a one-to-one physical decomposition of each error source.

Table 1 shows that the proposed concentrator maintains a high concentration ratio and acceptable spot quality for realistic levels of mirror deformation. When the RMS slope error is within $\sigma_s \leq 1$ mrad, the concentration ratio remains above approximately 93% of the nominal value, and the increase in RMS spot radius is limited to within about 22%. Even for σ_s = 2 mrad, the concentration ratio decreases by approximately 14%, and the focal spot still preserves a compact shape without severe fragmentation. Only when σ_s approaches 3 mrad does the concentration ratio exhibit a more pronounced decline and the focal spot become noticeably blurred. These sensitivity results indicate that the aberration-compensated off-axis design is robust against realistic mirror figure errors and compatible with the fabrication tolerances of lightweight space reflectors.

4. Experiment

To validate the optimized simulation results, a solar concentration experiment was conducted in an outdoor environment with a temperature of 5 °C and a solar irradiance of 390 W·m^{-2} (Fig. 7(a)). The setup included an optimized triple-reflector concentrator, a solar pyranometer, a solar tracking device, and an infrared thermal

Please cite this article as: Y. Zhang, P. Guo, M. Tian et al., A High-Efficiency Off-Axis Space Solar Concentrator with Large Tolerance for Acceptance Angle Variations, Engineering, https://doi.org/10.1016/j.eng.2026.08.029

Table 1
Sensitivity of optical performance to RMS mirror slope error σ_s (normalized to the ideal case).

σ_s(mrad)	Normalized concentration ratio	Normalized RMS spot radius	Normalized optical efficiency	Comment
0.0	1.00	1.00	1.00	Baseline, ideal mirrors
0.5	0.97	1.10	0.98	High-quality mirrors
1.0	0.93	1.22	0.96	Typical high-end concentrating solar power (CSP) mirrors
2.0	0.86	1.40	0.92	Upper bound of realistic deformation
3.0	0.78	1.65	0.88	Degraded mirrors/strong thermos–elastic distortion

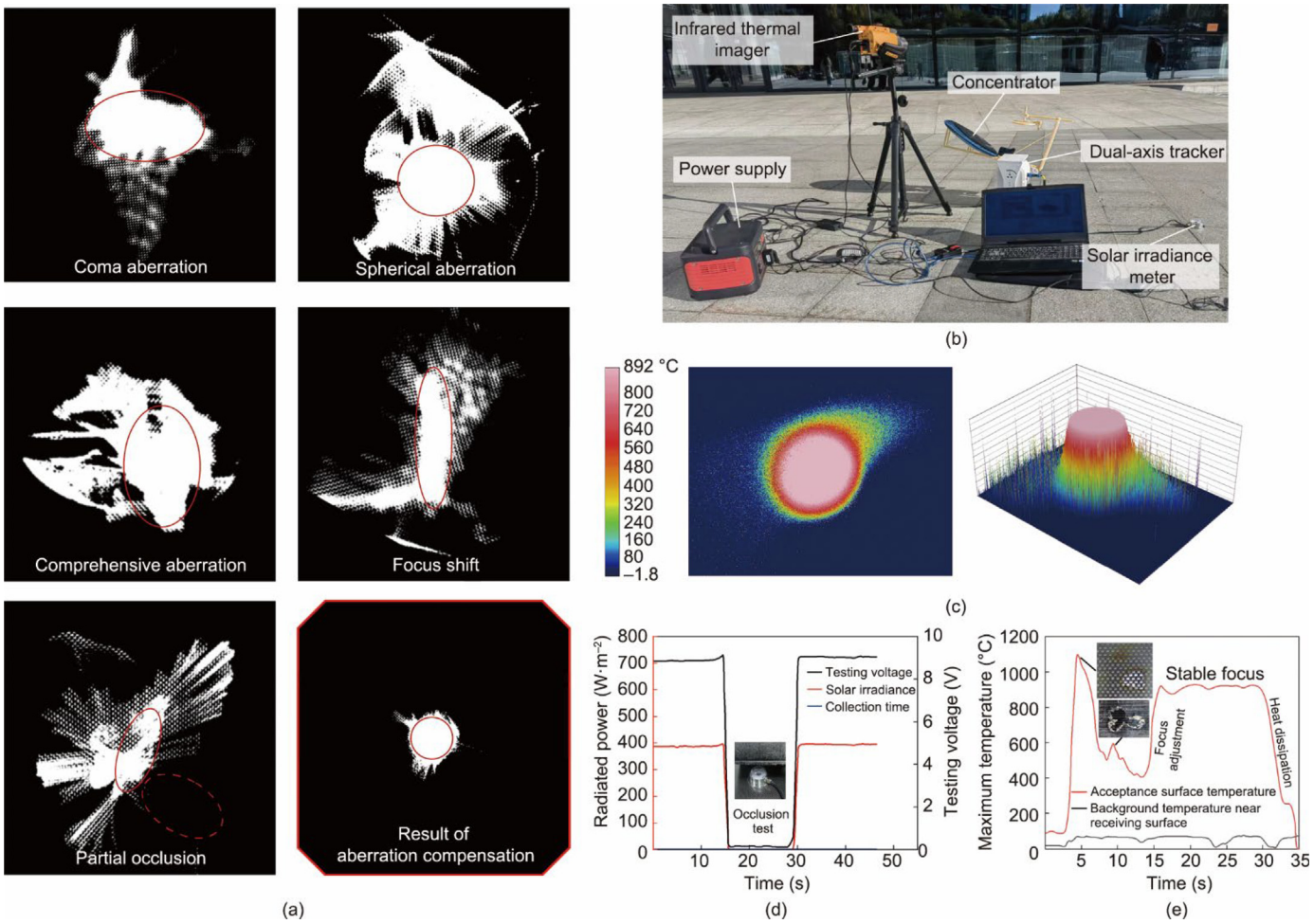


Fig. 7. Outdoor concentration experiment: (a) spot shapes generated by different off-axis concentrators; (b) overall layout of experimental setup; (c) temperature distribution of the focal point of the optimized concentrator; (d) calibration of actual solar irradiance; (e) temperature tracking process of the focal point of the optimized concentrator.

imager (Fig. 7(b)). The assembly followed a specific procedure: First, the reflective surfaces were cleaned, then aluminum foil was adhered using a backing adhesive, with the edges secured. The off-axis concentrator had an aperture of 300 mm, with its optical axis perpendicular to the standard plane of the solar tracker, which moved accordingly to track the sun.

To quantify the experimental uncertainty, the performance specifications of the instruments were taken into account. The focal temperature was monitored by a Fluke TiX650 infrared thermal imager, which provides a temperature accuracy of ±1 °C or 1% of the reading (whichever is greater) over the temperature range relevant to this study (Fig. 7 (c)). The solar irradiance was measured by an XM8580 pyranometer, whose maximum permissible error is ±7% of the reading and whose repeatability is better than ±5% according to the manufacturer's datasheet (Fig. 7 (d). Combining these contributions in quadrature gives an overall uncertainty of approximately ±9% for the measured solar irradiance. The receiving surface was a carbon-fiber plate coated with a graphite-based layer. According to the material datasheet and published measurements for graphite in the 8–14 μm infrared band, the hemispherical emissivity is in the range $\varepsilon = 0.85–0.95$ at 800–1500 °C. In the infrared camera, the emissivity parameter was set to 0.90, consistent with these values. A simple radiative-balance sensitivity analysis shows that the relative error in the inferred temperature due to emissivity uncertainty satisfies $\Delta T/T \approx \Delta\varepsilon/4\varepsilon$. Even for a conservative emissivity uncertainty of ±0.05, the resulting error in focal temperature below ±1.4% (i.e., below ±15 °C around 900–1300 °C), which is comparable to but not larger than the combined instrumental accuracy and run-to-run variability. Therefore, emissivity uncertainty has only a minor effect on the reported focal temperature and does not change the main conclusions. In the present experiments, three repeated heating runs

under similar clear-sky conditions yielded peak focal temperatures of 884, 892, and 879 °C (Fig. 7(c)), corresponding to a standard deviation of about 7 °C (≈0.8%). Taking into account both the instrument accuracy and run-to-run variability, the uncertainty of the reported peak focal temperature is conservatively estimated as ±10 °C, while the uncertainty of the optical concentration ratio is within ±10%.

Fig. 7(a) presents a set of black-and-white enhanced images of the spot under various conditions, which can be compared with the optimized results. The experimental results indicate that increasing the off-axis concentrator's light-receiving angle effectively corrected the transmission path of small-angle radiation. Using a conjugate mirror to offset the aberrations caused by the off-axis concentrator minimized their impact on the spot shape, as shown in Fig. 7(c). The receiving surface, with a radius of 10 mm, captured most of the sunlight. The highest temperature at the focal point reached 892 °C, with a stable heating temperature exceeding 800 °C, and the concentrator achieved a concentration ratio of 548, meeting the expected performance.

The black curve in Fig. 7(e) corresponds to the apparent background temperature in a small region around the focal spot, as reported by the infrared camera. The initial value (~5 °C) reflects the outdoor ambient condition, while the subsequent increase is caused by radiative heating of the surroundings and repeated calibration of the camera. Independent meteorological data indicated that the ambient air temperature during the test remained within (5 ± 1) °C. At 5 s, the focus was successfully adjusted, and the carbon fiber plate at the focal point was instantly burned through. Within the time period of 8–9 s, the receiving surface was cleared using a cardboard sheet, which was instantly burned through. After adjusting the focus, stable concentrated heating was achieved at the focal point during the time period of 16–28 s, demonstrating the practicality of the off-axis conjugate method.

To quantitatively place the proposed concentrator in the context of existing off-axis and secondary-reflector designs, Table 2 [18–20,22] compares representative systems reported in recent literature with the present work. For each configuration, the table lists the optical concept, the reported geometric or effective concentration ratio, and the approximate angular acceptance when available. Although the optical conditions and application targets differ among these systems, the comparison indicates that our off-axis conjugate point-focus design achieves a relatively high effective concentration ratio while maintaining an acceptance half-angle of ±0.5°, which is competitive with state-of-the-art off-axis and three-mirror concentrators designed for space or high-flux applications.

Because the outdoor experiments were conducted in standard terrestrial atmosphere, the measured focal temperature reflects the combined effect of solar input, radiative losses to the surroundings, convective cooling by the ambient air and conductive losses through the target holder. In contrast, on the lunar surface the absence of an atmosphere eliminates convective heat transfer, and the thermal balance at the receiving surface is dominated by radiation to the surroundings and conduction into the regolith. Therefore, the peak focal temperature of 892 °C obtained at 390 W·m^{-2} and 5 °C can be regarded as a conservative lower bound for the achievable temperature under the same optical concentration ratio in a vacuum environment.

To separate the optical performance from the thermal environment, the outdoor experiment is first used to characterize the effective optical concentration ratio C_R and absorptivity factor μ, which are independent of whether the system operates on Earth or on the Moon. The solar energy input to the receiving surface is:

$$P_{in} = I_{in} A_{out} \mu C_R \tag{25}$$

where P_{in} is the solar energy input to the receiving surface, I_{in} is the measured solar irradiance (390 W·m^{-2}), and A_{out} is the effective area of the receiving surface.

The radiation loss is calculated according to the Stefan-Boltzmann law:

$$P_{out} = \sigma_{SB} \varepsilon A_{out} \left(T_{foc}^4 - T_{env}^4 \right) \tag{26}$$

where P_{out} is the energy output from the receiving surface, σ_{SB} is the Stefan-Boltzmann constant (5.67×10^{-8} W·(m^{-2}·K^{-4})), ε is the emissivity, T_{foc} is the focal point temperature in Kelvin, T_{env} is the ambient temperature (278.15 K).

For the outdoor experiment, convective losses to the ambient air are present in addition to the radiative term in Eq. (26), so the measured peak temperature T_{foc} corresponds to a slightly larger absorbed solar power than that implied by radiation alone. When extrapolating to lunar operation, we neglect convection and assume that the dominant heat sink is radiation to the surroundings, so the steady-state focal temperature is obtained by equating absorbed solar power and radiative loss. A loss coefficient η is introduced to account for these factors.

$$I_{in} A_{out} \mu C_R \eta = \sigma_{SB} \varepsilon A_{out} \left(T_{foc}^4 - T_{env}^4 \right) \tag{27}$$

This relation provides a first-order radiative balance for estimating the focal temperature under different irradiation conditions, assuming the same optical efficiency and negligible convective heat losses. To estimate the potential performance

Table 2
Quantitative comparison of representative off-axis/secondary-reflector concentrators and the present work.

Reference	Optical configuration	Reported concentration ratio	Acceptance half-angle	Notes on application
Goldstein and Gordon [18]	Tailored off-axis parabolic dish with optimized secondary optics for high optical tolerance	≈300 (geometric)	≲0.2°	High-flux solar furnace; emphasis on optical tolerance and misalignment robustness
Gong et al. [19]	Two-stage large-aperture parabolic trough with adaptive secondary reflector	≈200–250 (effective, depending on angle)	≈0.3°–0.5°	Terrestrial CSP; focuses on incidence-angle modifier and daily-tracking behavior
Bellos and Tzivanidis [20]	Booster secondary reflector for parabolic trough collector	Up to ≈150–200 (geometric enhancement)	≈0.3°	Terrestrial trough collector; secondary booster improves concentration ratio (C_R) but with a limited field of view
Yang et al. [22]	Unobscured three-mirror anastigmatic off-axis optical system with low misalignment sensitivity	≈300 (geometric)	≲0.3°	General three-mirror off-axis concentrator/telescope; desensitized to misalignments
This work	Off-axis conjugate point-focus concentrator with triple-mirror, zero-occlusion layout	548 (effective concentration ratio)	±0.5° (acceptance half-angle)	Off-axis freeform mirrors plus conjugate compensation; tailored for lunar ISRU melting and space operation

Please cite this article as: Y. Zhang, P. Guo, M. Tian et al., A High-Efficiency Off-Axis Space Solar Concentrator with Large Tolerance for Acceptance Angle Variations, Engineering, https://doi.org/10.1016/j.eng.2026.08.029

under idealized lunar surface conditions, Eq. (27) is further evaluated using a solar irradiance of 1361 W·m^{-2} and an ambient surface temperature of 393 K. Using the experimentally calibrated C_R, and assuming unchanged optical efficiency and purely radiative heat exchange, the corresponding focal temperature is obtained as $T_{moc} \approx 1599$ K (1326 ℃). This value should be regarded as a theoretical projection for lunar conditions rather than a directly measured temperature.

$$I_{moon}A_{out}\mu C_R\eta = \sigma_{SB}\varepsilon A_{out}\left(T_{moc}^4 - T_{moon}^4\right) \tag{28}$$

where I_{moon} is the solar irradiance on the lunar surface, T_{moon} is the ambient temperature on the lunar surface, T_{moc} is the theoretically predicted focal temperature for this idealized lunar case.

In Eqs. (27) and (28), the focal temperature projected for an idealized lunar case is evaluated using $\varepsilon = 0.90$, which is a conservative lower-bound emissivity for graphite at high temperature. If ε is varied within 0.85–0.95, the predicted lunar focal temperature T_{moc} changes by less than ±2% (about ±25 °C around 1326 °C). This confirms that the projected focal temperature is weakly sensitive to the emissivity assumption and is dominated by the optical concentration rather than the exact surface radiative properties.

To further validate the optical design, the key performance metrics obtained from the MCRT simulations are compared with the outdoor concentration experiment. The main quantities and their discrepancies are summarized in Table 3.

5. Conclusions and discussion

This study introduces a novel off-axis conjugate solar concentrator tailored to the demands of lunar ISRU and solar-driven lunar regolith melting. The following key findings were obtained:

Aberration compensation and focusing efficiency: Aberrations were identified as the primary cause of focal spot deformation, which significantly reduces focusing efficiency. By integrating a conjugate mirror into the optical path, the dominant coma and spherical aberrations were effectively mitigated. The normalized total Seidel aberration index $\sum_{i=1}^{4}|S_i|$ on the receiving surface is reduced from 1.00 for the initial coaxial triple-mirror design to 0.04 after optimization, while precise control of the focal spot position is maintained and occlusion is eliminated through the optimized off-axis layout.

Enhanced tolerance and concentration performance: The concentrator demonstrated increased acceptance angles in edge regions, enabling a high tolerance to sunlight tracking deviations. Simulations showed that within an acceptance half-angle of ±0.5°, the focal spot approached a compact, near-circular spot, with RMS radius remaining below 10 μm. Experimentally, the concentrator maintained a high concentration ratio (> 300) and minimized the impact of tracking errors during field rotations.

Table 3
Comparison between simulated and measured performance of the optimized off-axis conjugate concentrator.

Quantity	Simulation	Experiment	Difference
Solar irradiance at aperture	1361 W·m^{-2}	390 W·m^{-2}	Different conditions
Optical concentration ratio	570	548 ± 55	−13.5%~+5.8%
Effective focal-spot diameter (x)	18	(23 ± 2) mm	+16.7%~+39%
Effective focal-spot diameter (y)	22	(27 ± 2) mm	+13.6%~+31.8%
Peak focal temperature	1421 °C	(892 ± 10) °C (390 W·m^{-2}) (1326 ± 15) °C (1361 W·m^{-2})	−7.7%~−5.6%

Stable high-temperature output: Under outdoor test conditions (solar irradiance of about 390 W·m^{-2} and an ambient temperature of 5 °C), the concentrator achieved a measured concentration ratio of 548 and sustained focal temperatures above 800 °C at the receiving surface. A simplified radiative balance model is used to extrapolate these results to a lunar surface irradiance of 1361 W·m^{-2}, suggesting that focal temperatures on the order of 1599 K would be attainable under idealized lunar conditions, which would be sufficient for regolith melting. These extrapolated values, while not measured directly in this work, indicate that the proposed concentrator has adequate thermal margin for future lunar ISRU applications.

Engineering feasibility and future prospects: The tolerance analyses in Sections 3.2 and 3.3 provide an indication of the engineering feasibility of the proposed concentrator. The slope-error sensitivity study shows that an RMS mirror slope error up to about 1 mrad on each reflective surface results in only approximately 3%–7% reduction in concentration ratio and keeps the RMS focal-spot radius below 26 μm, which is compatible with the figure accuracy routinely achieved by diamond-turned or precision-milled off-axis mirrors with replicated coatings. Likewise, the ±0.5° angular acceptance demonstrated in the field-of-view simulations implies that typical assembly misalignments and tracking errors on the order of ±0.2°–0.3° can be tolerated without severe performance degradation, easing the requirements on the dual-axis tracking system.

From a materials standpoint, the concentrator can employ space-qualified protected-silver or enhanced-aluminum coatings, whose solar-weighted reflectance remains above 0.9 after long-term ultraviolet and particle-radiation exposure according to existing space-mirror data. The peak heat flux at the receiving surface is of the order of 2×10^5 W·m^{-2}, which is below typical damage thresholds for such coated substrates, while the off-axis architecture keeps the mirrors themselves at comparatively moderate flux levels. Future work will include dedicated environmental tests of coated mirror coupons under ultraviolet radiation, electron/proton bombardment, and thermal-vacuum cycling to quantify long-term degradation in a lunar-like environment, as well as structural analyses of the support framework under launch and deployment loads.

This work underscores the potential of advanced solar concentrator systems in supporting sustainable ISRU processes and, together with the radiative extrapolation to lunar conditions, lays the groundwork for their application in constructing long-term lunar infrastructure.

CRediT authorship contribution statement

Yanlong Zhang: Writing – review & editing, Writing – original draft, Visualization, Validation, Software, Methodology, Investigation, Formal analysis, Data curation, Conceptualization. **Pengzhen Guo:** Writing – review & editing, Supervision, Resources, Project administration, Funding acquisition, Conceptualization. **Mengfan Tian:** Validation. **Yun Chen:** Validation. **Zin Min Khant:** Validation. **Yiming Kong:** Validation. **Dingkun Gao:** Validation. **Linghao Li:** Validation. **Hongwei Guo:** Resources, Funding acquisition. **Rongqiang Liu:** Resources, Project administration, Funding acquisition, Formal analysis. **Zongquan Deng:** Resources, Project administration, Funding acquisition. **Lifang Li:** Writing – review & editing, Supervision, Resources, Project administration, Funding acquisition, Formal analysis, Conceptualization.

Declaration of competing interest

The authors declare that they have no known competing financial interests or personal relationships that could have appeared to influence the work reported in this paper.

Please cite this article as: Y. Zhang, P. Guo, M. Tian et al., A High-Efficiency Off-Axis Space Solar Concentrator with Large Tolerance for Acceptance Angle Variations, Engineering, https://doi.org/10.1016/j.eng.2026.08.029

Acknowledgments

This work was financially supported in part by the National Key R&D Program of China (2025YFF0511402), the National Natural Science Foundation of China (52675316, 52275241, and 52575272), the State Key Laboratory of Space Environment and Matter Interaction Foundation, the National Key Laboratory of Aerospace Mechanism Foundation, the National Key Laboratory of Laser Spatial Information Foundation (LSI2025ZZKY02), and the Chinese Academy of Engineering-funded Academic Project: Chinese Academy of Engineering Science and Technology Seminar—Innovative Development of Space Intelligent Robots and Mechanisms (2026-XS-04).

References

[1] Shichalin O, Belov A, Buravlev I, Kolodeznikov E, Fedorets A, Lembikov A, et al. Additive manufacturing development of construction materials for a lunar base via spark plasma sintering of volcanic rocks using *in-situ* resource utilization concept. Constr Build Mater 2024;442:137553.
[2] Liu H, Yao Z, Liu H. Human lunar base: "Lunar Palace 1" team of Beihang University unveils China's "Lunar Palace" plan. Innovation 2024;5(2):100592.
[3] Wang G, Zhang Z, Lin J. Multi-energy complementary power systems based on solar energy: a review. Renew Sustain Energy Rev 2024;199:114464.
[4] Gargari LS, Joda F, Ameri M, Nami H. Optimization and exergoeconomic analyses of water–energy–carbon nexus in steel production: integrating solar–biogas energy, wastewater treatment, and carbon capture. Int J Hydrogen Energy 2024;86:275–92.
[5] Rathore SKP, Sikarwar SB. Thermal energy storage using phase change material for solar thermal technologies: a sustainable and efficient approach. Sol Energy Mater Sol Cells 2024;277:113134.
[6] Liu Y, Gui Q, Xiao L, Zheng C, Zhang Y, Chen F. Photothermal conversion performance based on optimized design of multi-section compound parabolic concentrator. Renew Energy 2023;209:286–97.
[7] Wu G, Yang Q, Fang H, Zhang Y, Zheng H, Zhu Z, et al. Photothermal/day lighting performance analysis of a multifunctional solid compound parabolic concentrator for an active solar greenhouse roof. Sol Energy 2019;180:92–103.
[8] Mazarico E, Neumann GA, Smith DE, Zuber MT, Torrence MH. Illumination conditions of the lunar polar regions using LOLA topography. Icarus 2011;211(2):1066–81.
[9] Zhang Y, Liu B, Di K, Liu S, Yue Z, Han S, et al. Analysis of illumination conditions in the lunar south polar region using multi-temporal high-resolution orbital images. Remote Sens 2023;15(24):5691.
[10] Vasavada AR, Bandfield JL, Greenhagen BT, Hayne PO, Siegler MA, Williams JP, et al. Lunar equatorial surface temperatures and regolith properties from the Diviner Lunar Radiometer Experiment. J Geophys Res 2012;117:E00H18.
[11] Sefton-Nash E, Siegler MA, Paige DA. Thermal extremes in permanently shadowed regions at the lunar south pole. In: Proceedings of 44th Lunar and Planetary Science Conference; 2013 Mar 18–22; The Woodlands, TX, USA. Universities Space Research Association; 2013.
[12] Gläser P, Sanin A, Williams JP, Mitrofanov I, Oberst J. Temperatures near the lunar poles and their correlation with hydrogen predicted by LEND. J Geophys Res 2021;126(9):e2020JE006598.
[13] Vishnu SK, Senthil R. Experimental performance and economic analysis of finned solar receiver for parabolic dish solar collector. Heliyon 2023;9(11):e21236.
[14] Zhang X, Hou X, Wang L, Yan Y. Investigation of light concentrating mode for SSPS. China Space Sci Technol 2016;36(2):1–12. Chinese.
[15] Zhang X, Zhang Y, Zheng C, Chen F. Model construction and performance investigation of compound parabolic concentrator based on satellite solar wing photovoltaic arrays. Energy 2023;285:129398.
[16] Yu Q, Dai G, Yang C, Peng L, Wang M, Chen X. Bi-level multi-objective optimization of the structure and attitude for space solar power station. Adv Space Res 2024;73(3):1952–65.
[17] Carrington C, Feingold K, Howell J. Space solar power concepts: demonstrations to pilot plants. In: Proceedings of 53rd International Astronautical Congress; 2002 Oct 10–19; Houston, TX, USA. NASA Technical Reports Server; 2002.
[18] Goldstein A, Gordon MJ. Tailored solar optics for maximal optical tolerance and concentration. Sol Energy Mater Sol Cells 2011;95(2):624–9.
[19] Gong J, Wang J, Lund DP, Hu E, Xu Z, Liu G, et al. Improving the performance of a 2-stage large aperture parabolic trough solar concentrator using a secondary reflector designed by adaptive method. Renew Energy 2020;152:23–33.
[20] Bellos E, Tzivanidis C. Investigation of a booster secondary reflector for a parabolic trough solar collector. Sol Energy 2019;179:174–85.
[21] Wu S, Wang C, Tang R. Optical efficiency and performance optimization of a two-stage secondary reflection hyperbolic solar concentrator using machine learning. Renew Energy 2022;188:437–49.
[22] Wang Y, Li Y, Gu Z, Fu Y. Optical design method of a three-mirror anastigmatic telescope with low misalignment sensitivity based on the nodal aberration theory. Appl Opt 2022;61(22):6483–91.
[23] Dähler F, Wild M, Schäppi R, Haueter P, Cooper T, Good P, et al. Optical design and experimental characterization of a solar concentrating dish system for fuel production via thermochemical redox cycles. Sol Energy 2018;170:568–75.
[24] Rodriguez-Sanchez D, Rosengarten G. Optical efficiency of parabolic troughs with a secondary flat reflector; effects of non-ideal primary mirrors. Energy 2024;288:129521.
[25] Memme S, Fossa M. A novel approach for incidence angle modifier calculation of arbitrarily oriented linear Fresnel collectors: theory, simulations and case studies. Renew Energy 2024;222:119857.
[26] Boccalatte A, Fossa M, Ménézo C. Calculation of the incidence angle modifier of a Linear Fresnel Collector: the proposed declination and zenith angle model compared to the biaxial factored approach. Renew Energy 2022;185:123–38.
[27] Meng Q, Wang H, Wang W, Yan Z. Desensitization design method of unobscured three-mirror anastigmatic optical systems with an adjustment–optimization–evaluation process. Appl Opt 2018;57(6):1472–81.
[28] Li J, Ding Y, Cai Y, Yuan G, Zhang M. Optimization method for low tilt sensitivity of secondary mirror based on the nodal aberration theory. Appl Sci 2022;12(13):6514.
[29] Ren C, Meng Q. Design method for freeform off-axis three-mirror anastigmat optical systems with a large field of view and low error sensitivity. Photonics 2024;11(3):211.
[30] Duan Z, Li Z, An W. Design and preliminary experiment of an off-axis aequilate-mirrors linear Fresnel concentrator with sunlight self-adaptive feature. Appl Therm Eng 2024;257:124401.
[31] Artal P, Fernández E, Manzanera S, Piers P. Adaptive-optics system to predict the impact of aberrations in the quality of vision. Invest Ophthalmol Vis Sci 2002;43(13):2064.
[32] Tan H, Xia X, Liu L, Ruan L. Numerical calculation of infrared radiation characteristics and transmission–computational thermal radiation. Harbin: Harbin Institute of Technology Press; 2006. Chinese.
[33] Wu H, Luo C, Zhang X, Ge P, Zhang X. Design of a freeform reflector for LED sources based on a feedback method. Light Res Technol 2016;48(3):365–75.
[34] Meng X. Optical adjustment design of reflecting solar concentrator and energy conversion analysis of CPVT system [dissertation]. Harbin: Harbin Institute of Technology; 2017. Chinese.
[35] Li L, Zhang Y, Li H, Liu R, Guo P. An optimized approach for solar concentrating parabolic dish based on particle swarm optimization-genetic algorithm. Heliyon 2024;10(4):e26165.

Please cite this article as: Y. Zhang, P. Guo, M. Tian et al., A High-Efficiency Off-Axis Space Solar Concentrator with Large Tolerance for Acceptance Angle Variations, Engineering, https://doi.org/10.1016/j.eng.2026.08.029